Monthly Notices
of the
ROYAL ASTRONOMICAL SOCIETY

MNRAS **453,** 3375–3385 (2015) doi:10.1093/mnras/stv1863

Observations of free–free and anomalous microwave emission from LDN 1622 with the 100 m Green Bank Telescope

S. E. Harper,[1]★ C. Dickinson[1] and K. Cleary[2]

[1]*Jodrell Bank Centre for Astrophysics, Alan Turing Building, School of Physics and Astronomy, The University of Manchester, Oxford Road, Manchester, M13 9PL, UK*
[2]*Cahill Center for Astronomy and Astrophysics, California Institute of Technology, Pasadena, CA 91125, USA*

Accepted 2015 August 11. Received 2015 August 11; in original form 2015 January 7

ABSTRACT

LDN 1622 has previously been identified as a possible strong source of dust-correlated anomalous microwave emission (AME). Previous observations were limited by resolution meaning that the radio emission could not be compared with current generation high-resolution infrared data from *Herschel*, *Spitzer* or *Wide-field Infrared Sky Explorer*. This paper presents arcminute resolution mapping observations of LDN 1622 at 4.85 and 13.7 GHz using the 100 m Robert C. Byrd Green Bank Telescope. The 4.85 GHz map reveals a corona of free–free emission enclosing LDN 1622 that traces the photodissociation region of the cloud. The brightest peaks of the 4.85 GHz map are found to be within ≈10 per cent agreement with the expected free–free predicted by Southern H-Alpha Sky Survey Atlas Hα data of LDN 1622. At 13.7 GHz, the AME flux density was found to be 7.0 ± 1.4 mJy and evidence is presented for a rising spectrum between 13.7 and 31 GHz. The spinning dust model of AME is found to naturally account for the flux seen at 13.7 GHz. Correlations between the diffuse 13.7 GHz emission and the diffuse mid-infrared emission are used to further demonstrate that the emission originating from LDN 1622 at 13.7 GHz is described by the spinning dust model.

Key words: radiation mechanisms: general – dust, extinction – diffuse radiation – ISM: individual objects: LDN 1622 – photodissociation region (PDR) – radio continuum: ISM.

1 INTRODUCTION

Dust-correlated anomalous microwave emission (AME) has been observed in the frequency range 10–60 GHz and has a spectrum distinct from other sources of Galactic emission in the same range, such as free–free, synchrotron and the cosmic microwave background (CMB; Kogut et al. 1996; Leitch et al. 1997; de Oliveira-Costa et al. 2004; Gold et al. 2011). Evidence of AME has been found in molecular clouds (Watson et al. 2005; Casassus et al. 2008; Planck Collaboration XX 2011), H II regions (Dickinson et al. 2009; Tibbs et al. 2012), Lynds dark clouds (Casassus et al. 2006; AMI Consortium et al. 2009), large-scale diffuse Galactic dust (Peel et al. 2012) and in one external galaxy (Murphy et al. 2010). As AME is present in many different environments, it may become an important new tool for studying the interstellar medium (ISM).

There have been several proposed mechanisms for AME. The spinning dust model is currently the favoured explanation for AME (Draine & Lazarian 1998a,b). The other possible explanations for AME include: free–free emission from shock-heated gas (Leitch et al. 1997); flat spectrum synchrotron emission (Bennett et al. 2003) and magnetic dipole emission from dust grains (Draine & Lazarian 1999). For the purposes of this paper, the spinning dust model is assumed to be the origin of AME. The spinning dust model proposes that the rapid rotation of small dust grains with electric dipoles generates AME (Draine & Lazarian 1998a,b; Ali-Haïmoud, Hirata & Dickinson 2009; Hoang, Draine & Lazarian 2010; Ysard, Miville-Deschênes & Verstraete 2010). Dust grains in the ISM can be broadly separated into big grains (BGs; > 0.1 μm), very small grains (VSGs; < 0.1 μm) and disc-like molecules known as polyaromatic hydrocarbons (PAHs; as small as tens of atoms; Desert, Boulanger & Puget 1990; Li & Draine 2001). VSGs generate mid-infrared (MIR) continuum emission, whereas PAHs are observed as several MIR emission bands between 1 and 12 μm (Tielens 2008). The spinning dust model assumes that only the VSGs and PAHs contribute to AME. Therefore, strong morphological correlations are expected between AME and MIR emission.

Recent *Planck* observations have identified numerous possible AME sources within the Galaxy that can be described by the spinning dust model (Planck Collaboration XV 2014). The *Planck* observations also provided strong evidence in support of previous observations of the Perseus (Watson et al. 2005) and ρ-Ophiuchus (Casassus et al. 2008) molecular clouds as bright AME sources (Planck Collaboration XX 2011). However, it is still unknown whether PAHs or VSGs contribute the most towards the generation of AME. By observing AME at resolutions comparable to

★ E-mail: stuart.harper@manchester.ac.uk

current infrared space observatories, such as *Wide-field Infrared Sky Explorer* (*WISE*), *Spitzer* and *Herschel*, it should be possible to determine the dust grain population generating AME.

A full-width half-maximum (FWHM) resolution of 1 arcmin or smaller would be required to compare radio observations with infrared (IR) data from current IR observatories such as *Spitzer* and *Herschel*. These resolutions are easily obtainable using interferometric radio observations. However, AME has a largely extended and diffuse morphology and interferometers are only sensitive to particular angular scales. Typically, if the angular size of a source extends beyond the primary beam resolution of the interferometer, the flux from the larger angular scales is lost (Thompson, Moran & Swenson 2007). Interferometers can lack sensitivity to extended emission as not all scales are observed. Single-dish radio observations are able to measure all the flux from a source. This makes single-dish observations are potentially very suited to measuring diffuse and extended sources. A difficulty with single-dish observations is that they require extremely large apertures in order to achieve resolutions comparable to the IR observatories. The 100 m Robert C. Byrd Green Bank Telescope (GBT) is one of the few radio telescopes with a dish large enough to reach FWHM resolutions smaller than $\approx$1 arcmin.

Lynds dark cloud LDN 1622 is a starless cometary cloud in the vicinity of the Orion B molecular cloud, north-east of Barnard's Loop (Maddalena et al. 1986). The west and south sides of LDN 1622 are traced by a bright Hα corona that is clearly visible in the Southern H-Alpha Sky Survey Atlas (SHASSA) images (Gaustad et al. 2001) and is illuminated by the nearby Ori OB1b stellar association (Kun et al. 2008). The bright Hα corona may also trace the photodissociation region (PDR) around LDN 1622. The Cosmic Background Interferometer (CBI) observed LDN 1622 at 31 GHz with an 8 arcmin synthesized beam and found a strong correlation between the emissions from the PDR seen by CBI 31 GHz and *IRAS* 12 μm (Casassus et al. 2006). The IR correlations seen by CBI were attributed to heated VSGs within the PDR generating AME. Earlier observations of LDN 1622 over 5–10 GHz with the 140 ft GBT also identified LDN 1622 as possibly one of the first compact sources of AME (Finkbeiner et al. 2002). Evidence for AME was also found by the CBI at 31 GHz in the nearby cloud LDN 1621 (L1621), which is approximately 30 arcmin north of LDN 1622 (Dickinson et al. 2010). The proximity of LDN 1621 to LDN 1622 suggests they may share similar grain populations and therefore if AME is found in one cloud it may be present in the other.

This paper presents new observations of LDN 1622 at 4.85 (*C* band) and 13.7 GHz (*Ku* band) taken with the GBT. These are the first extended mapping of a Lynds dark cloud with high resolution radio observations from a single-dish radio telescope. This paper is structured as follows: Section 2 discusses the observations, data processing and ancillary data. Section 3 describes the GBT maps of LDN 1622. Section 4 compares the emissions seen at 4.85 and 13.7 GHz by the GBT to archival and ancillary observations of LDN 1622. Finally, Section 5 summarizes the findings in this paper.

2 OBSERVATIONS AND DATA PROCESSING

2.1 GBT observations

The GBT is a 100 m diameter fully steerable single-dish radio telescope that operates at frequencies less than 100 GHz. The observations were taken over several days in 2007 January and one extra observation was made the following year in 2008 January. The observed time on source for *C* band was 5 and for *Ku* band 7.5 h.

Observations were made at two frequencies: 4.85 (*C* band) and 13.7 GHz (*Ku* band). Both *C*-band and *Ku*-band observations used the Digital Continuum Receiver (DCR) on the GBT. The observations used all the 16 frequency channels available to the DCR for each frequency, this provided a bandwidth of 1.28 GHz for *C* band and 3.5 GHz for *Ku* band. The sample integration time was 0.2 s. The *C*-band receiver has a single beam with an FWHM resolution of 2.6 arcmin at 4.85 GHz. At *Ku* band, the GBT has two receivers with independent beams, both with an FWHM resolution at 13.7 GHz of 55 arcsec. One receiver is located in the central focal position of the GBT and will be referred to in this paper as the central beam. The other *Ku*-band receiver is displaced by 330 arcsec in the cross-elevation direction and will be referred to as the off-centre beam. Both *C* band and *Ku* band operated in dual polarization mode, measuring left (LL) and right (RR) circularly polarized radiation simultaneously. It was assumed that the emission from LDN 1622 would have negligible circular polarization, therefore total intensity could be obtained by averaging together the LL and RR data.

On-the-fly (OTF) mapping was used to scan across the regions in right ascension (RA) and declination (Dec.), at a speed on the sky of 1 arcmin s^{-1}. This resulted in a series of nested scans across both regions. The *C*-band observations mapped a region of 35 arcmin $\times$ 35 arcmin centred upon LDN 1622 at RA $=5^{\rm h}54^{\rm m}29^{\rm s}$, Dec. $=1^{\circ}45'36''$. The *Ku*-band observations mapped a 12 arcmin $\times$ 12 arcmin subregion of LDN 1622 centred upon RA $=5^{\rm h}54^{\rm m}16^{\rm s}$ and Dec. $=1^{\circ}49'52''$. In order to obtain the desired total integration time per beam in the final map, multiple scans of the same region were made. The choice to use nested OTF observations helped to reduce the effect of time-correlated $1/f$ noise caused by the atmosphere or receivers.

The theoretical thermal noise of the receiver was calculated using (GBT Proposers Guide 2015):

$$\left(\frac{\sigma}{\rm mK}\right) = \frac{44.2}{\mu}\frac{\left(\frac{T_{\rm sys}}{\rm K}\right)}{\sqrt{\left(\frac{\Delta\nu}{\rm GHz}\right)\left(\frac{\tau}{\rm s}\right)}}, \quad (1)$$

where $T_{\rm sys}$ is the measured system temperature, $\Delta\nu$ is the bandwidth of the receiver, τ is the sample integration time and μ is the aperture efficiency. The aperture efficiency for *C* band was 75 and for *Ku* band 72 per cent. The theoretical noise levels were 2.34 and 2.1 mK for *C* band and *Ku* band, respectively. The measured median noise level for all the *C*-band and *Ku*-band scans were 16.9 and 13.0 mK. Comparing the median noise level to the theoretical noise level for *C* band and *Ku* band revealed that the measured noise was 7.2 and 6.2 times higher, respectively. The higher than expected noise for both frequencies was due to $1/f$ noise contamination in the data. Reducing the effect of $1/f$ noise on the data is discussed in the following section.

2.2 Calibration and processing

The internal noise diode of the receiver, with a known equivalent antenna temperature for each receiver ($T_{\rm cal}$), was used to calibrate the time-ordered data (TOD) into units of brightness temperature using the following equation:

$$T_{\rm b} = \frac{T_{\rm cal}}{2}\frac{V_{\rm on}+V_{\rm off}}{\langle V_{\rm on}-V_{\rm off}\rangle} - \frac{T_{\rm cal}}{2}. \quad (2)$$

The noise calibration diode was injected into every other sample in the TOD at a frequency of 5 Hz. $V_{\rm on}$ describes the receiver voltage

when the noise diode was on and $V_{\rm off}$ describes the receiver voltage when the noise diode was off.

To check the diode calibration, the flux densities of 3C161, 3C48 and 3C147 were measured at the beginning and half-way through each observing session. The measured flux densities based on the diode calibration were then compared to the predicted flux densities from the source models described in Ott et al. (1994). The flux densities of 3C161, 3C48 and 3C147 measured at *C* band and *Ku* band after calibrating with the diode were all found to be within 5 per cent of the predicted flux densities.

The opacity of the atmosphere at radio wavelengths is dependent on the water vapour content of the air and the elevation of the observation. Over the several days of observing the relative humidity varied considerably, between 0 and 90 per cent, and the elevation of the observations varied by 10°. Measurements of zenith opacity from weather stations near to the GBT were used to estimate the effect of atmospheric opacity on the data. The maximum attenuation was estimated to be <0.05 and <2.6 per cent for *C* band and *Ku* band. As these corrections are less than the flux density calibration accuracy, no atmospheric absorption corrections were applied to either *C* band or *Ku* band.

The emission from ground-based radar and geostationary TV satellites peak at around the *C*-band and *Ku*-band frequencies. These terrestrial sources of radio emission are considered radio frequency interference (RFI) and completely dominate astronomical sources. Several scans were found to be RFI contaminated. These scans were identified by comparing the peak signal in each scan to the thermal noise limit of the receiver. Scans containing any source with a brightness greater than 20 times the receiver noise were flagged as RFI contaminated and removed.

Time-correlated noise within the TOD caused by the gain fluctuations in the receiver amplifiers or the instability of atmospheric water vapour can increase the effective noise of the TOD to be many times higher than the receiver thermal noise limit. This type of noise is known as $1/f$ noise due to the effect it has on the shape of the TOD power spectrum. The spectrum of $1/f$ can be approximated by a power law (Seiffert et al. 2002):

$$P_\nu = \sigma_w^2 \left[1 + \left(\frac{\nu_{\rm knee}}{\nu}\right)^\alpha\right], \tag{3}$$

where σ_w describes the thermal noise, $\nu_{\rm knee}$ is the knee frequency and α is the spectral index of the $1/f$ noise. At the knee frequency, the TOD thermal noise and low-frequency $1/f$ noise contribute equally to the spectral density of the TOD. The spectral index describes the power of the $1/f$ noise, with typical values range between 1 and 2.

When OTF mapping continuum sources, $1/f$ noise can cause stripes in the scan directions of the final map and obscure the astronomical signal. The effect of $1/f$ noise is a limitation of single-dish radio observations. However, there are methods for mitigating $1/f$ noise both during the observations and when data processing.

During the observations, the effect of $1/f$ noise on the astronomical signal was reduced by slewing the telescope as fast as possible. The data in each scan can be assumed to have $1/f$ noise contributions from the receiver and the atmosphere. The noise of each scan was assumed to have a fixed knee frequency. By slewing the telescope faster, the time for a scan can be made shorter than the time-scale of the $1/f$ noise variations. The limit on how much $1/f$ noise can be removed in this way is a balance between the knee frequency of the noise and the physical constraints of the telescope. In the case of these observations, the GBT could not slew fast enough to remove all the $1/f$ noise contamination.

During the data processing stage, scans containing high levels of $1/f$ noise contamination were removed. The ratio between the variance of pairs of data separated by two different lags was used as the metric to determine the $1/f$ contamination of a scan. The variance σ_τ^2 of a scan can be estimated from the variance of differenced sample pairs separated by a time-scale of τ using,

$$\sigma_\tau^2 = \frac{1}{2}\frac{\sum_{i=0}^{N-\tau}(d_{i+\tau} - d_i)^2}{N-\tau}, \tag{4}$$

where d_i and $d_{i+\tau}$ are the sample TOD at time i and time $i+\tau$, respectively. The median knee frequency of the data was found to be ≈0.7 Hz, which corresponds to a time-scale of $\tau = 1.4$ s. Differencing the TOD on shorter time-scales reduces the $1/f$ noise contribution to the total noise of the TOD. The estimate of the thermal white-noise level of the TOD was determined from the variance of pairs differenced by $\tau = 0.2$ s (1 sample). An estimator for the TOD $1/f$ contribution was determined from a differenced TOD with a lag of $\tau = 1.0$ s, which is slightly shorter than the median $1/f$ time-scale. Therefore the variance of the lagged differenced TOD would only deviate from the white-noise variance for scans with a high $1/f$ contribution. The ratio between the lagged differenced TOD standard deviation and the white-noise limit was measured for each scan as

$$R = \frac{\sigma_\tau}{\sigma_{\rm W}}. \tag{5}$$

The metric R defines the ratio of the lagged differenced TOD standard deviation (σ_τ) and the white-noise limit ($\sigma_{\rm W}$). If a scan exceeded a cut-off value for R it was discarded. Many different cut-off values for R were used to generate difference maps of the data. The optimal cut-off for R was determined when the noise in the difference maps was at a minimum. A value of 2.3 for R was found to minimize the noise in the difference maps at both frequencies. For *C* band and *Ku* band, 50 and 14 per cent of the scans exceeded the $R = 2.3$ maximum cut-off noise variance ratio and were removed.

A summary of the observations and map noise limits can be found in Table 1.

Table 1. Receiver and observational properties of the 4.85 (*C* band) and 13.7 GHz (*Ku* band) data sets.

Central frequency (GHz)	4.85	13.7
Bandwidth (GHz)	1.28	3.5
No. beams	1	2
Back end	DCR	DCR
Observing mode	On the fly	On the fly
Hours observed (h)	5	7.5
Beam (FWHM)	2.6 arcmin	55 arcsec
Smoothed beam (FWHM)	3 arcmin	1.2 arcmin
Sky scan speed (arcmin s^{-1})	1	0.5
Data flagged (per cent)	50	14
Map noise (mJy $beam^{-1}$)	4.3	5.5
Confusion limit[a] (mJy $beam^{-1}$)	≈0.45	≈0.03
Map noise (mK)	2.5	2.5
Confusion limit[a] (mK)	≈0.9	≈0.05
Field width (arcmin)	35	12

Note. [a]Confusion limit calculated using

$$\frac{\sigma_{\rm c}}{\rm mJy\,beam^{-1}} = 0.2\left(\frac{\nu}{\rm GHz}\right)^{-0.7}\left(\frac{\theta}{\rm arcmin}\right)^2, \tag{6}$$

which is a parametrized form of the calculation found in Condon (1974).

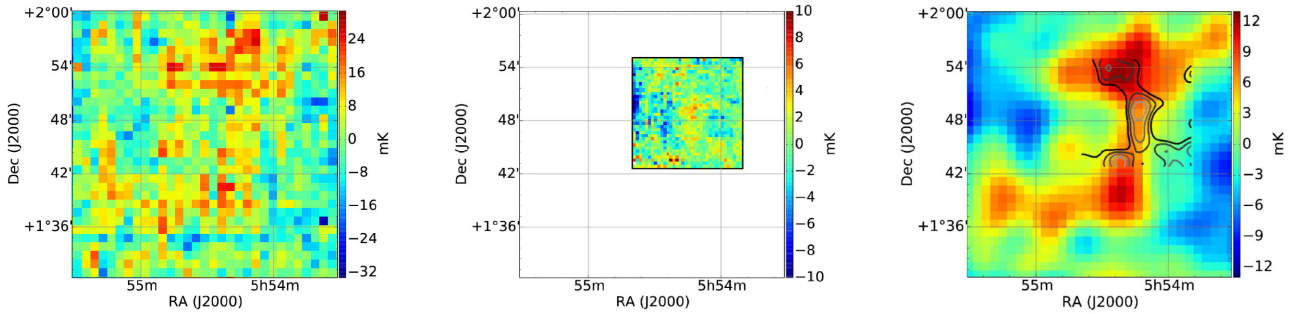

Figure 1. Final *C*-band and *Ku*-band maps as generated by the ML map-making method. The images are centred at RA $=5^{h}54^{m}29^{s}$, Dec. $=1^{\circ}45'36''$ with dimensions 30 arcmin×30 arcmin. Left: *C*-band map at the original 2.6 arcmin FWHM resolution. Centre: *Ku*-band map at the original 55 arcsec FWHM resolution. The black box marks the extent of the area observed by the central beam. Right: overlay of smoothed *Ku*-band map contours on the smoothed *C*-band map. The contour levels are 0.1, 0.45, 0.8, 1.15, 1.5 and 1.85 mJy beam^{-1} for a 1.2 arcmin beam.

2.3 Map making

The maximum-likelihood (ML) map-making technique was used as the final step in reducing $1/f$ in the final maps. ML map making was originally developed for CMB experiments as a way of recovering the weak CMB signal from $1/f$ noise dominated observations (Borrill 1999; Natoli et al. 2001; Doré et al. 2001). ML map making is the ideal method to use for these observations as for many scans the emission from LDN 1622 was dominated by $1/f$ noise.

The advantage of ML map making is that it uses an estimated full covariance matrix of the noise to find an optimal solution for the signal in the TOD. The estimated covariance matrix accounts for both the instrumental and atmospheric contributions to the $1/f$ noise. The work in this paper used an independently developed ML map maker. The ML map makers ability to recover signal from a $1/f$ contaminated set of TOD was tested using simulations. A summary of the ML map-making technique, this implementation and simulations are described in Appendix A.

2.4 Description of ancillary data

In this paper, the GBT data at *C* band and *Ku* band were compared with existing data at radio, IR and optical frequencies. Section 3.2 discusses the ancillary data and its relationship to the emissions at *C* band and *Ku* band in more detail.

Ancillary interferometric radio data at 15.7 GHz were provided by the Arcminute Microkelvin Imager (AMI) (Perrot, private communication; Zwart et al. 2008). The AMI Small Array (SA) consists of 10 3.7 m diameter dishes. The AMI SA has baseline spacings between 5 and 20 m and a synthesized beam of 3 arcmin.

FIR observations were obtained from publicly available archival European Space Agency *Herschel Space Observatory* (Pilbratt et al. 2010) data. The archival data were SPIRE (Griffin et al. 2010) and PACS (Poglitsch et al. 2010) photometry of Orion B at 500, 350, 250 and 160 μm. The FWHM resolutions of each band were approximately: 35.2, 23.9, 17.6 and 11.7 arcsec. The SPIRE and PACS observations were made in parallel mode with observation identification numbers OBSID: 1342205074 and OBSID: 1342205075. The *Herschel* maps were reduced using the SPG v11.1.0 pipeline. For the PACS data, the level 2.5 MADMAP products were used. The SPIRE level 2 products with an absolute background correction applied from *Planck* data were used. PACS 70 μm data were also available but were not used because of poor signal to noise.

MIR data were provided by the *WISE* (Wright et al. 2010). In this paper, only the 22 and 12 μm observations were used in order to reduce the number of point sources contaminating the field. The FWHM resolution of the *WISE* 22 μm map is 12 arcsec and the *WISE* 12 μm map is 7.4 arcsec.

An archival *Spitzer* IRAC (Fazio et al. 2004) map of LDN 1622 at 8 μm was used to supplement the *WISE* MIR data. Point sources from the *Spitzer* map were subtracted. The IRAC 8 μm map has an FWHM resolution of ≈1.98 arcsec.

Optical Hα data of LDN 1622 were taken from the SHASSA (Gaustad et al. 2001). The SHASSA Hα data serve as a tracer for the free–free emission seen at *C* band (Dickinson, Davies & Davis 2003). The SHASSA map has an FWHM resolution of 0.8 arcmin and can detect sources down to the level of ≈2 Rayleigh. The SHASSA continuum-subtracted maps contain numerous stellar artefacts around poorly subtracted bright sources. However, no significant stellar artefact contamination of the Hα emission observed around LDN 1622 was visible.

3 RESULTS

3.1 GBT maps

Fig. 1 presents the final *C*-band and *Ku*-band ML maps, both unsmoothed and smoothed. The unsmoothed *C*-band map has an FWHM resolution of 2.6 arcmin. The map pixel size for the *C*-band map is 57.6 arcsec ensuring 2.7 pixels across a beam. The pixel size was chosen to maintain Nyquist sampling across the field. The noise in the *C*-band map was estimated by generating a difference map from the RR and LL polarization data. The difference map should contain only the white noise and residual receiver $1/f$ noise. The pixel noise was sampled from a 20 arcmin diameter aperture in the centre of the difference map. The pixel noise within the aperture was measured to be 2.5 mK or 4.3 mJy beam^{-1}.

The *Ku*-band map is shown alongside the *C*-band map in Fig. 1. The original resolution of the *Ku*-band map was 55 arcsec FWHM and the map has 2.7 pixels per beam FWHM with a pixel size of 20.5 arcsec. As with the *C*-band map, the pixel size was chosen to ensure Nyquist sampling across the map. The *Ku*-band analysis only used data that fell within the field of view of the central *Ku*-band feed, from either the central or offset *Ku*-band feeds. This region is marked by a box in Figs 1 and 2. Data that fell within the regions observed only by the offset *Ku*-band feed were omitted principally due to these regions having a far higher contribution

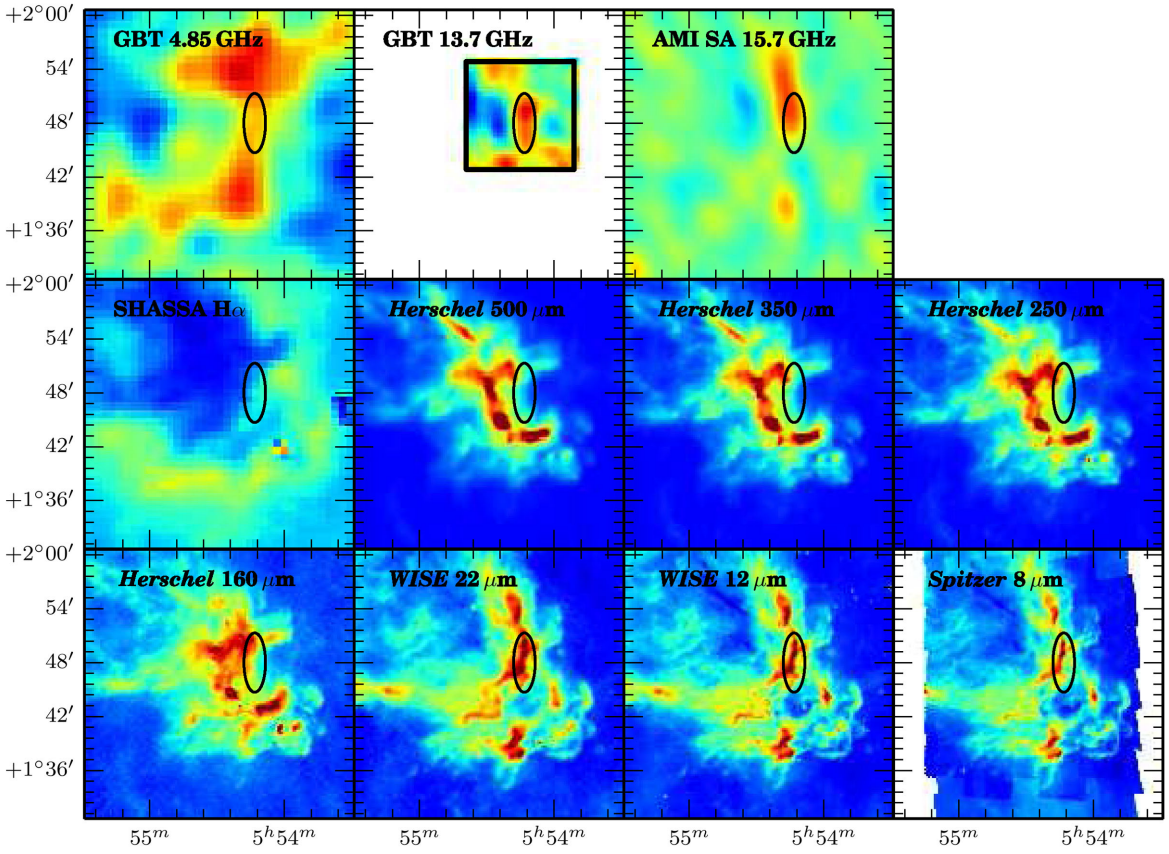

Figure 2. Maps of LDN 1622 from GBT *C*-band and *Ku*-band observations and ancillary data. Each image is centred at RA $=5^{\rm h}54^{\rm m}29^{\rm s}$, Dec. $=1^\circ45'36''$ with dimensions of 30 arcmin×30 arcmin. The elliptical aperture in each map marks the peak in *Ku*-band emission. A box surrounds the region observed by the central *Ku*-band beam in the *Ku*-band map. From the top left to the bottom right the images are: GBT *C*-band 4.85 GHz smoothed to a 3 arcmin beam and *Ku*-band 13.7 GHz smoothed to a 1.2 arcmin beam; AMI 15.7 GHz Small Array; SHASSA Hα; *Herschel* SPIRE 500, 350 and 250 μm; *Herschel* PACS 160 μm; *WISE* 22 and 12 μm; *Spitzer* IRAC 8 μm.

of noise. Additionally, much of the area observed by offset feed was displaced by several beamwidths from the *Ku*-band source of interest. The higher noise level of the offset *Ku*-band regions is due to the observing strategy displacing the offset feed scans over a larger area of sky than the area observed by the central feed. The pixel noise in the *Ku*-band map was sampled from a 6 arcmin diameter aperture in a difference map, generated from the two circular polarizations, centred on the *Ku*-band source marked in Fig. 2. The noise was found to be 2.5 mK or 5.5 mJy beam^{-1}.

Fig. 1 also shows smoothed contours of the *Ku*-band map overlaid on to a smoothed *C*-band map. The *Ku*-band map was smoothed to 1.2 arcmin FWHM resolution and the *C*-band map was smoothed to 3 arcmin FWHM resolution. The smoothing kernel for both GBT maps was chosen to increase signal to noise while retaining the structure of the emission within the field. The noise level of the smoothed *C*-band map is 1.7 mK or 2.9 mJy beam^{-1} and the noise level of the smoothed *Ku*-band map is 0.8 mK and 1.8 mJy beam^{-1}.

3.2 Comparison with multifrequency data

In Fig. 2, the smooth *C*-band and *Ku*-band maps are shown alongside ancillary maps of LDN 1622.

The *C*-band free–free emission in Fig. 2 can be seen to enclose LDN 1622 in a corona which spans from the south-east to the north-west and arches towards the south-west corner of the map. The Hα emission, a known tracer of free–free emission (e.g. Dickinson et al. 2003), can also be seen to have formed a corona of emission with a similar morphology to the corona of *C*-band emission. A key feature in the *C*-band and Hα maps is the southern bar that spans the cloud east to west. This feature seems to correlate quite well between the *C*-band and Hα maps. The rest of the corona shows significant differences in morphology between the Hα and *C*-band emission, which can be mostly attributed to dust absorption of the Hα emission. Corrections for dust absorption are discussed in more detail in Section 4.1.

The corona, seen as both free–free and Hα emission, is likely associated with warm H II gas within the photodissociation region (PDR) around LDN 1622. The PDR around LDN 1622 is a transitional region, where on the western side gas and dust are heated and ionized by far-ultraviolet (FUV) radiation. Progressing eastward the FUV flux is absorbed and the gas and dust eventually cool into the atomic and molecular phases (Hollenbach & Tielens 1999). The FIR and MIR structures shown in the *Herschel*, *WISE* and *Spitzer* maps around the aperture marked in Fig. 2 clearly show the separate stages occurring within the PDR. The MIR maps are tracing the emission from the warm VSGs, which are mixed with the ionized H II gas, as shown by the *C*-band data, and are exposed to the ionizing interstellar radiation field. PDRs are environments rich in PAH molecules that have emission lines which lie within

the passbands of the *WISE* 12 μm and *Spitzer* 8 μm maps (Tielens 2008). At longer wavelengths, such as in the FIR *Herschel* maps, the maps trace the location of cooler dust. The cooler dust is located in clumps near the core of LDN 1622 where the dust is shielded from the interstellar radiation field and is in thermal equilibrium with the environment.

In the smoothed *Ku*-band map, an elongated structure can be seen running north–south through the marked aperture in Fig. 2. The location of this aperture was also the location of the peak in emission seen at 31 GHz by CBI (Casassus et al. 2006). The weak emission from the elongated structure at *Ku* band is also clearly visible in Fig. 2 AMI 15.7 GHz SA map. Comparing the *Ku*-band map with the MIR maps reveals a shared morphology in the region of the aperture. The correlations between the MIR and *Ku*-band maps implies a possible common source. The spinning dust model provides a possible explanation for the shared MIR and *Ku*-band morphology as it provides a mechanism for PAH molecules to emit at the *Ku*-band frequency (Ali-Haïmoud et al. 2009; Ysard et al. 2010). A more detailed discussion of the *Ku*-band emission and its correlations with IR and radio emission can be found in Section 4.2.

Note that a bright young stellar object (YSO) at RA $=5^{\rm h}54^{\rm m}24.3^{\rm s}$ and Dec. $=1^{\circ}44'19''$ was removed from the FIR and MIR maps. The YSO has been briefly discussed in Bally et al. (2009) and is associated with the protostellar outflow HH 962.

4 ANALYSIS AND DISCUSSION

4.1 Free–free emission from LDN 1622

Ionized regions of H II gas generate both H α and free–free continuum emission. The brightness of H α emission is directly proportional to the density of the ionized hydrogen ($n_{\rm H}$) and the rate at which recombination occurs within the cloud, resulting in the H α transition. The brightness of free–free emission depends on the density of free electrons ($n_{\rm e}$) and ions within a region. In H II regions, the free electrons are generated via ionization therefore it is expected that $n_{\rm e} \approx n_{\rm H}$. Both emissions also depend on the electron temperature of the region, which is typically $T_{\rm e} \approx 10^4$ K. As both free–free and H α emissions share a common source, it is possible to directly relate the brightness of one emission to the brightness of the other (e.g. Dickinson et al. 2003).

In Fig. 2, both the *C*-band and SHASSA maps show the same corona of H II tracing the south and west edges of LDN 1622. The differences in the morphology of the radio free–free and SHASSA H α emissions around LDN 1622 are primarily due to optical dust absorption of the H α emission. Correcting for H α dust absorption is complicated as the distribution of dust and H II gas is unknown. In this section, the radio free–free emission is estimated from the SHASSA map using the method outlined in Dickinson et al. (2003) and compared with the observed *C*-band free–free emission. The extinction of the H α by dust is estimated using a simple radiative transfer model and optical depths measured from the *Herschel* FIR maps.

FIR *Herschel* data of LDN 1622 were used to estimate H α absorption, $A({\rm H}\,\alpha)$. The first step in deriving $A({\rm H}\,\alpha)$ was to smooth all the *Herschel* maps to a common resolution. The 353 GHz optical depth (τ_{353}) was fitted for, pixel by pixel, over four *Herschel* bands. Each pixel was fitted with the modified blackbody curve:

$$S_\nu = B_\nu(T_{\rm D})\tau_{353}\left(\frac{\nu}{353\,{\rm GHz}}\right)^{\beta}, \quad (7)$$

where β, the emissivity index, the dust temperature, $T_{\rm D}$, and τ_{353} were all free parameters. B_ν is a blackbody curve dependent on the dust temperature.

IR optical depth was converted to hydrogen column density ($N_{\rm H}$) using:

$$\tau_{353} = \sigma_{e\,353} N_{\rm H}, \quad (8)$$

where $\sigma_{e\,353}$ is the mean whole sky dust opacity derived by *Planck* (Planck Collaboration XI 2014). The hydrogen column density was then related to extinction ($E(B-V)$) by assuming the relationship $N_{\rm H}/E(B-V) \approx 6.94 \times 10^{21}$ cm^{-2} (Planck Collaboration XI 2014). The H α absorption factor was related to the measured extinction with,

$$A({\rm H}\,\alpha) = 0.81 R(V) E(B-V). \quad (9)$$

The reddening value ($R(V)$) for the ISM is typically ≈3.1 (Schultz & Wiemer 1975; Sneden et al. 1978). However, $R(V)$ is observed to increase in denser regions of the ISM and even vary significantly between the edge of a dark cloud and its interior with a range of reddening values between $3.5 < R(V) < 5.5$ (Vrba & Rydgren 1985, 1984). Considering the typical reddening values of other dark clouds and that LDN 1622 is quite a translucent cloud, a nominal reddening value of $R(V) = 4$ was assumed.

The expected H α emission ($I_{\rm em}$) was estimated from the observed H α emission ($I_{\rm obs}$) by applying the following H α absorption model pixel by pixel to the SHASSA map:

$$I_{\rm obs} = \frac{I_{\rm em}}{\tau}\int_0^{f\tau} {\rm e}^{\tau'-\tau}{\rm d}\tau' + (1-f)I_{\rm em}. \quad (10)$$

The H α optical depth (τ) was related to H α absorption by $\tau = A({\rm H}\alpha)/(2.5\log_{10}(e))$. The H α absorption model assumed that a certain fraction (f) of the H II gas and dust were mixed and in thermal equilibrium, while the remaining fraction of H II gas was in front of the dust and its H α emission unabsorbed. The model does not consider H II gas completely behind the dust within LDN 1622 because the H α emission in that case would be mostly absorbed resulting in large uncertainties in the estimated radio free–free. However, it is possible that some fraction of H II gas is completely obscured by dust behind LDN 1622.

After correcting for H α absorption, the H α brightness was converted to the equivalent radio free–free brightness using the method described in Dickinson et al. (2003). The derived H α to radio free–free conversion factor, assuming an electron temperature of $T_{\rm e} = 7000$ K, was 0.28 mK R^{-1} at 4.85 GHz. The final simulated free–free map was smoothed to an FWHM of 3 arcmin to match the smoothed *C*-band resolution. The median background of the simulated free–free map was subtracted to represent the effect of the map-making process removing the zero level of the *C*-band data.

Three examples of simulated free–free maps with dust–gas mixing fractions of $f = 0.1$, 0.5 and 1.0 are shown in Fig. 3 with *C*-band contours overlaid. At low mixing fractions, visual inspection of the H α and *C*-band maps shows that both contain the same large-scale coronal structure. However, some bright H α regions and smaller scale structures within the corona, such as in the western region of the H α map, deviate from the observed free–free emission. The expected brightness of the *C*-band free–free emission estimated from the H α map agree with observations within approximately 10 per cent at low mixing fractions. At higher mixing fractions, a bright core of emission forms in the west of the simulated LDN 1622 corona that is completely unrepresentative of the observed *C*-band emission. This implies that there is possibly very little dust–gas mixing occurring in the south of LDN 1622. The morphology and

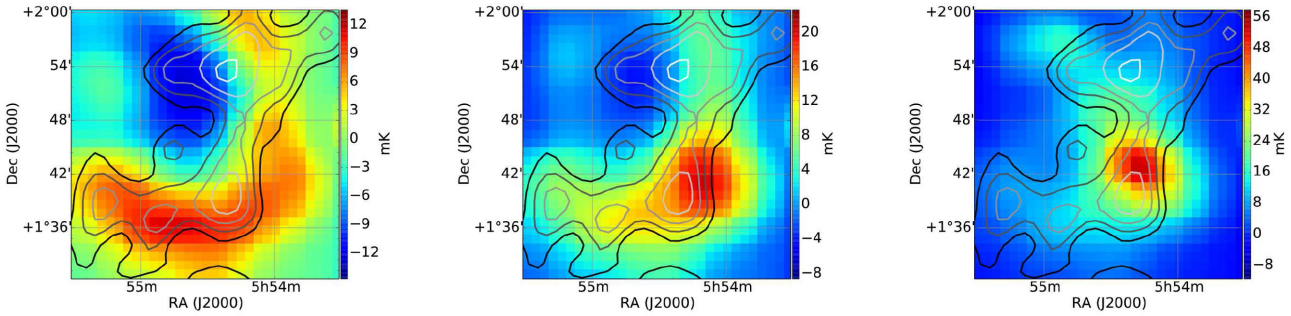

Figure 3. Overlay of smoothed *C*-band contours on H α derived free–free maps assuming an electron temperature of 7000 K. The contour levels are 1, 3.75, 6.5, 9.25 and 12 in units of mK. The dust mixing fraction for each map from left to right is: $f = 0.1$, 0.5 and 1.0.

brightness of the north-west region of the corona appears significantly different in the predicted free–free maps to the observed *C*-band emission. The brightest region of the *C*-band emission in the north-west region of the corona is offset towards the east of the predicted free–free emission. An explanation for this is that much of the H II gas generating the free–free emission is behind the dust in LDN 1622, therefore the H α emission has been completely absorbed along that line of sight.

The discrepancies between the observed *C*-band emission and simulated free–free emission could be explained by the dust–gas mixing fraction (f) varying across the cloud. It is possible that changes in the dust–gas mixing fraction is not the only explanation. The model assumed that both the 353 GHz dust opacity ($\sigma_{e\,353}$) and optical reddening value ($R(V)$) were both constant across LDN 1622. However, IR dust opacity and reddening are both linked to grain size distributions, which could be changing from the edge of LDN 1622 towards the core (Weingartner & Draine 2001).

The comparison between the SHASSA H α and CBI 31 GHz observations of LDN 1622 (Casassus et al. 2006, fig. 9) did not show any emission originating from the north-western part of the corona that can be seen as a bright feature in the *C*-band map. Therefore, an upper limit of 16.7 mK on the free–free emission was estimated from the contours of the CBI map. This upper limit implies that the measured brightness range of the *C*-band emission between 6 and 11 mK is plausible.

To summarize, the emission detected at *C* band is seen to trace the H II corona of LDN 1622 and broadly agrees with the morphology of the SHASSA H α map. The peak free–free brightness predicted by the H α emission agrees within $\approx$10 per cent of the peak observed *C*-band free–free emission for the bright H α ridge in the south of LDN 1622 for dust mixing fractions of $f \lesssim 0.1$. From these *C*-band observations, the precise cause for the differences in morphology and brightness between the expected and observed free–free emission remains unknown. Possible explanations are variations in the local dust–gas mixing fraction, reddening value or IR dust opacity over LDN 1622. These explanations cannot satisfactorily explain the emergence of the bright core in the expected free–free emission at high mixing fractions, as seen in Fig. 3. The high noise level in the *C*-band maps will also be a significant contribution to the differences in expected and observed free–free morphology and brightness across the LDN 1622 corona.

4.2 AME at *Ku* band

Aperture photometry of the AME in LDN 1622 was performed using the ellipse centred on the peak emission in the smoothed *Ku*-band map shown in Fig. 2. The central coordinates of the aperture ellipse are RA $=5^{\rm h}54^{\rm m}13^{\rm s}$, Dec. $=1^{\circ}47'49''$. The aperture ellipse has a semimajor axis of 3 arcmin and a semiminor axis of 1.25 arcmin.

Visual inspection of Fig. 2 shows that there is some contribution of free–free emission from H II gas as well as MIR emission from dust grains within the aperture. This section will determine whether the emission at *Ku* band is AME or just free–free emission. This required calculating the expected free–free emission flux at *Ku* band and assessing whether there is any significant morphological similarities between the emissions at *Ku* band and the MIR.

Aperture photometry was used to measure the flux within the *Ku*-band aperture shown in Fig. 2. The aperture size of 3 arcmin $\times$ 1.25 arcmin was chosen by expanding the aperture axes from zero until the signal-to-noise ratio within the aperture was maximized. The uncertainty within the *Ku*-band aperture was estimated from an elliptical annulus. The annulus had inner and outer semiminor axes of 2.17–4.68 arcmin and inner and outer semimajor axes of 5.2–11.2 arcmin. The central coordinates of the annulus were the same as the aperture coordinates. The annulus inner and outer axes were chosen to enclose a sufficiently large sample of pixels from the *C*-band and *Ku*-band maps. Due to the *Ku*-band source being in close proximity to a number of diffuse sources, the estimated uncertainty on the flux density was measured from a difference map that splits the data between the first days and the last days of observing. By differencing different days, the difference map contained a statistically similar $1/f$ noise contribution from the atmosphere and receivers as the *Ku*-band map. A 5 per cent systematic uncertainty from the calibration of the data were added in quadrature to the measured uncertainties of the *C*-band and *Ku*-band flux densities. No correction for background emission was performed when calculating the flux density at *Ku* band or *C* band to avoid additional uncertainties due to poor constraints on the background emission. The mean background temperature of both the *Ku*-band and *C*-band maps were 0 mK due to the map-making process.

The flux density within the *Ku*-band aperture shown in Fig. 2 was measured as 7.0 ± 1.4 mJy. The flux density within the same aperture at *C* band was found to be 5.8 ± 2.4 mJy, which corresponds to an expected free–free flux density at 13.7 GHz of 5.0 ± 2.0 mJy assuming a free–free spectral index of -0.15. The corresponding fractional AME excess at 13.7 GHz was found to be 0.29 ± 0.13.

The measured fluxes from LDN 1622 were compared to the expected AME fluxes predicted by the spinning dust model and

INTERACTIVE DATA LANGUAGE code SPDUST (Ali-Haïmoud et al. 2009; Silsbee, Ali-Haïmoud & Hirata 2011). The SPDUST model expects nine environment parameters in order to estimate the expected AME flux from a region. The following is a brief description of each environment parameter and its value: the hydrogen number density ($n_{\rm H} = 10^4$ H cm^{-3}), the gas temperature ($T = 22$ K), relative intensity of interstellar radiation field ($\chi = 10^{-4}$), hydrogen ionization fraction ($x_{\rm H} = 1$ ppm), carbon ionization fraction ($x_{\rm C} = 1$ ppm), fractional abundance of molecular hydrogen ($y = 0$), H_2 formation rate ($\gamma = 0$), rms of the dipole moment for dust grains ($\beta = 9.3$) and the grain size distribution parameters corresponding to a given line in Weingartner & Draine (2001, table 1, Line 7). A more detailed discussion of the SPDUST environment parameters can be found in Ali-Haïmoud et al. (2009).

In this paper, the dark cloud environment parameters from Draine & Lazarian (1998b) are used. The expected hydrogen number density for a dark cloud was checked against a calculated estimate of the true hydrogen number density for LDN 1622. The distance to LDN 1622 is typically considered to be similar to the Orion molecular clouds (≈400 pc) and it has an approximate angular size of 13 arcmin. Assuming the cloud is spherical and using the measured mean column density from *Herschel* FIR data ($\approx 1.5 \times 10^{22}$ H cm^{-2}), the estimated hydrogen number density was found to be ≈3000 H cm^{-3}, implying that the typical dark cloud $n_{\rm H} = 10^4$ H cm^{-3} is a reasonable order of magnitude estimate for LDN 1622. The gas temperature parameter was matched to the mean dust temperature ($T_{\rm D}$) within the *Ku*-band aperture derived from the *Herschel* FIR data, $T = T_{\rm D} = 22 \pm 2$ K.

A key indication of spinning dust is a rising spectrum between ≈10–30 GHz. The expected flux density within the *Ku*-band aperture at 31 GHz was estimated using the CBI contours shown in Casassus et al. (2006) and scaling the flux density, assuming a smooth source, to the expected flux within just the *Ku*-band aperture. The spectral index between 13.7 and 31 GHz was found to be 2.3 ± 0.2, where the spectral index is defined by the simple power-law relationship,

$$S_2 = S_1 \left(\frac{\nu_2}{\nu_1}\right)^{\alpha}, \tag{11}$$

where S_1 and ν_1 are the *Ku*-band flux density and frequency of 7.0 ± 1.4 mJy and 13.7 GHz, respectively, S_2 and ν_2 are the derived CBI flux density and frequency of 44.3 ± 1.4 mJy and 31 GHz, and α is the spectral index. The uncertainty in the spectral index was estimated using,

$$\sigma_\alpha = \frac{1}{\ln(\frac{\nu_2}{\nu_1})} \sqrt{\left(\frac{\sigma_1}{S_1}\right)^2 + \left(\frac{\sigma_2}{S_2}\right)^2}, \tag{12}$$

where ν is a given frequency, S is the flux density at a given frequency and σ is the measured flux density uncertainty. The spectral index derived from SPDUST between the same frequencies is 1.84, which is 2.6σ from the measured spectral index. The strong confirmation that the spectral flux density spectrum is rising between 13.7 and 31 GHz and the agreement with the rising spectral index predicted by SPDUST is a good indication that spinning dust is present within LDN 1622 in the region of the *Ku*-band aperture.

A map of LDN 1622 using the AMI SA at 15.7 GHz was provided for the purposes of visual comparison with the *Ku*-band map. Fig. 4 shows the AMI SA data overlaid with *Ku*-band contours. As both observations are at similar frequencies, and both observations are sensitive to similar large-scale structures there should be significant correlations between the AMI SA and *Ku*-band maps. Both the map and contours in Fig. 4 share the same large-scale elongated north–south structure. The most significant difference between the map and contours in Fig. 4 is the small displacement of the *Ku*-band GBT data towards the west.

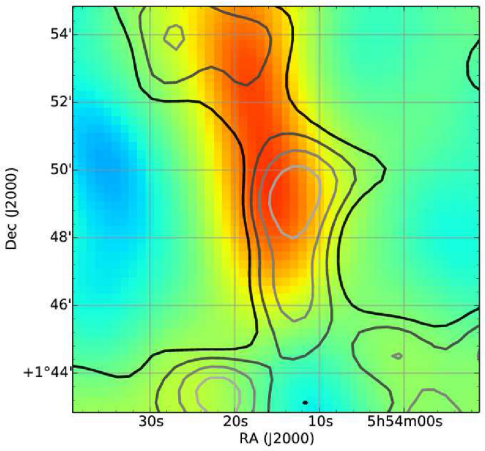

Figure 4. Overlay of smoothed GBT *Ku*-band contours on AMI SA colourscale. The contours are in units of mJy beam^{-1}, with a beam FWHM of 1.2 arcmin. The contour levels are 0.1, 0.45, 0.8 and 1.15 mJy beam^{-1}.

It was shown in the previous discussion that the flux at *Ku* band can be naturally accounted for by the spinning dust model and that there is a clear rising spectrum between 13.7 and 31 GHz indicative of AME. However, if spinning dust is the origin of the *Ku*-band emission there should be significant correlations between *Ku*-band and MIR emission. The spinning dust model predicts that PAH molecules, VSGs or a combination of both are the source of AME. VSGs generate MIR continuum emission and PAH molecules emit bright MIR emission lines at 12.7, 11.3, 8.6 and 7.7 μm (Tielens 2008). The *WISE* 12 μm and *Spitzer* 8 μm passbands encompass these four PAH emission lines. The *WISE* 22 μm passband only contains MIR continuum emission from the VSGs. Therefore, if PAH molecules contribute to the generation of AME, there should be a larger morphological correlation between the *Ku* band and the 12 and 8 μm maps than with the 22 μm map. It should be noted that it has been suggested that MIR emission in some H II regions and PDRs could be due to the formation of second-generation BGs in these environments (Everett & Churchwell 2010; Draine 2011; Paladini et al. 2012). There is a possibility that second-generation BGs are contributing to the MIR emission inside the PDR around LDN 1622, especially as the measured dust temperature within the PDR is quite warm, $T_{\rm D} = 22$ K. However, for this paper BGs were assumed to not be contributing to the observed MIR emission.

In order to correlate the diffuse emission at *Ku* band with the diffuse emission in the MIR, the MIR maps had to first be filtered of point sources. For both the *WISE* and *Spitzer* maps a number of point sources near to the elongated north–south structure were patched out. The patching process involved replacing the source with a second-order polynomial and noise estimated from the background around the source. Due to the shorter wavelength and higher resolution of the *Spitzer* map, there were a much larger number of weaker visible point sources, which were then removed using a median filter.

The patching and median filtering of the point sources left a number of artefacts in the diffuse structure of the MIR maps at scales comparable to the FWHM resolutions of the MIR maps. However, it is reasonable to assume that these artefacts had minimal effect on

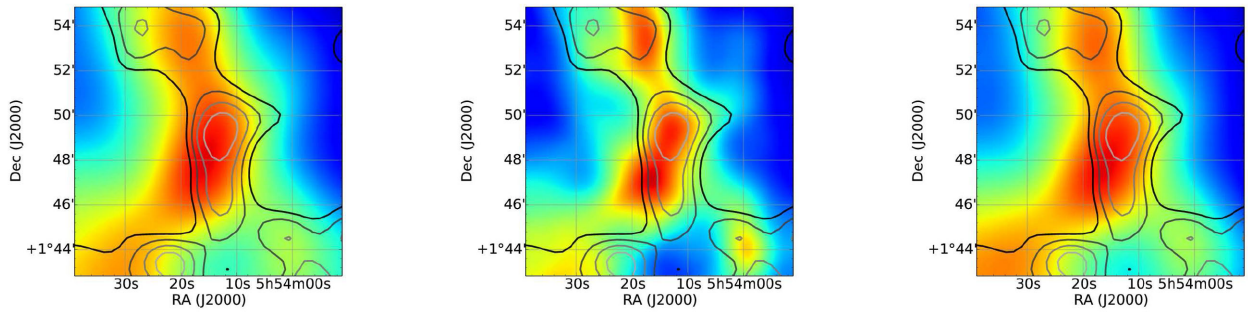

Figure 5. Overlay of smoothed *Ku*-band contours on the smoothed, point source removed MIR maps. Left: *WISE* 22 μm, centre: *WISE* 12 μm, right: *Spitzer* IRAC 8 μm. The contour levels are 0.1, 0.45, 0.8 and 1.15 mJy beam^{-1} for a 1.2 arcmin beam.

this analysis as all the MIR maps were smoothed considerably to match the 1.2 arcmin FWHM resolution of the smoothed *Ku*-band map.

The 1.2 arcmin FHWM, point source filtered *WISE* and *Spitzer* maps are shown in Fig. 5 with *Ku*-band contours overlaid. All three maps and the contours share the similar elongated north–south morphology. All the maps in Fig. 5 reveal that the peak in MIR emission also coincides with the location of the peak *Ku*-band emission. From visual comparison of the MIR maps with the *Ku*-band contours, there is no clear indication that either the *Spitzer* 8 μm or *WISE* 12 μm maps, which contain the PAH emission lines, have stronger correlations with the *Ku*-band contours than the MIR continuum emission seen in the *WISE* 22 μm map.

The Pearson's correlation coefficient, r, between the *Ku*-band map and each MIR map was measured to quantify any morphological correlations between the maps. The pixels in the maps were made quasi-independent by matching the pixel size to the FWHM of the maps. The Pearson correlations for each MIR map with the *Ku*-band map were found to be: r (22 μm) $= 0.54 \pm 0.13$, r (12 μm) $= 0.59 \pm 0.13$ and r (8 μm) $= 0.49 \pm 0.13$. The uncertainties in r were estimated by bootstrapping the data and using the Fisher's r to z transform (Fisher 1915). The Pearson correlation measurements imply that there is a slightly higher correlation between the *Ku*-band and the MIR maps containing PAH emission lines. However, the uncertainties on the correlation coefficients reveal there is no significantly higher correlation between the *Ku*-band map and any one MIR map.

In summary, this section finds evidence to support the possibility that spinning dust in the form of either VSGs or PAHs is generating AME within the PDR of LDN 1622. Comparing the *C*-band and *Ku*-band data alone finds a small excess of emission at *Ku* band at the 2σ level. However, a rising spectrum indicative of AME was found when comparing the flux densities at 13.7 and 31 GHz. Finally, morphological correlations between the *Ku*-band and MIR emissions lends further support to the presence of AME within LDN 1622.

5 CONCLUSION

This paper has presented arcminute resolution mapping observations of the diffuse radio emission associated with LDN 1622 at *C* band and *Ku* band using the 100 m GBT. The goal of the observations was to measure free–free emission in the LDN 1622 region and identify and confirm the origin of the AME measured by previous observations.

A free–free corona associated with the PDR of LDN 1622 was revealed in the *C*-band maps. The emission seen in the SHASSA Hα map was converted into the expected free–free brightness temperatures at *C* band and the peak brightnesses were found to agree within ≈10 per cent of the peak observed *C*-band emission. However, much of the Hα emission around LDN 1622 was shown to be affected by significant dust extinction. A simple model of the effect of dust extinction on the Hα emission was shown to be not sufficient to correct for Hα absorption over the whole cloud.

The *Ku*-band observations show a weak north–south elongated source inside the PDR of LDN 1622. The diffuse nature of the *Ku*-band emission made measurements of the flux density difficult. However, a weak source at the core of an elongated structure was identified. The flux density of the source was found to be consistent with previous observations of LDN 1622 and the flux density predicted by the spinning dust model of AME. Evidence was found for a rising spectrum between the measured GBT 13.7 GHz emission and CBI 31 GHz emission, a strong indicator of spinning dust. Finally, the overall morphological structure of the *Ku*-band emission was found to weakly correlate with the emission from VSGs and PAH molecules at MIR wavelengths. It should be acknowledged that the emission at *Ku* band is very weak and that the *C*-band observations do not entirely exclude the possibility that the emission at *Ku* band is at least partially free–free emission. However, the correlations of the *Ku*-band emission with MIR and ancillary radio data, along with the measured rising spectrum of the source, do give reasonable confidence that the observed 13.7 GHz emission from LDN 1622 is mostly spinning dust driven AME.

ACKNOWLEDGEMENTS

SH acknowledges support from an STFC-funded studentship. CD acknowledges support from an STFC consolidated grant (ST/L000768/1), an STFC Advanced Fellowship, an EU Marie-Curie IRG grant under the FP7 and an ERC Starting (Consolidator) Grant (no. 307209). The authors would like to thank Roberta Paladini, Simon Casassus and Tim Pearson for helpful discussion and comments. The authors would also like to thank Yvette Perrott and the MRAO AMI group for providing the AMI SA observation of LDN 1622.

REFERENCES

Ali-Haïmoud Y., Hirata C. M., Dickinson C., 2009, MNRAS, 395, 1055
AMI Consortium et al., 2009, MNRAS, 400, 1394
Bally J., Walawender J., Reipurth B., Megeath S. T., 2009, AJ, 137, 3843
Bennett C. L. et al., 2003, ApJS, 148, 1

Casassus S., Cabrera G. F., Förster F., Pearson T. J., Readhead A. C. S., Dickinson C., 2006, ApJ, 639, 951
Casassus S. et al., 2008, MNRAS, 391, 1075
Condon J. J., 1974, ApJ, 188, 279
de Oliveira-Costa A., Tegmark M., Davies R. D., Gutiérrez C. M., Lasenby A. N., Rebolo R., Watson R. A., 2004, ApJ, 606, L89
Desert F.-X., Boulanger F., Puget J. L., 1990, A&A, 237, 215
Dickinson C., Davies R. D., Davis R. J., 2003, MNRAS, 341, 369
Dickinson C. et al., 2009, ApJ, 690, 1585
Dickinson C. et al., 2010, MNRAS, 407, 2223
Doré O., Teyssier R., Bouchet F. R., Vibert D., Prunet S., 2001, A&A, 374, 358
Draine B. T., 2011, ApJ, 732, 100
Draine B. T., Lazarian A., 1998a, ApJ, 494, L19
Draine B. T., Lazarian A., 1998b, ApJ, 508, 157
Draine B. T., Lazarian A., 1999, ApJ, 512, 740
Everett J. E., Churchwell E., 2010, ApJ, 713, 592
Fazio G. G. et al., 2004, ApJS, 154, 10
Finkbeiner D. P., Schlegel D. J., Frank C., Heiles C., 2002, ApJ, 566, 898
Fisher R. A., 1915, Biometrika, 10, 507
Gaustad J. E., McCullough P. R., Rosing W., Van Buren D., 2001, PASP, 113, 1326
GBT Support Staff, 2015, GBT Proposers Guide, The Proposers Guide for the Green Bank Telescope, available at: https://science.nrao.edu/facilities/gbt/facilities/gbt/proposing/GBTpg.pdf
Gold B. et al., 2011, ApJS, 192, 15
Griffin M. J. et al., 2010, A&A, 518, L3
Hoang T., Draine B. T., Lazarian A., 2010, ApJ, 715, 1462
Hollenbach D. J., Tielens A. G. G. M., 1999, Rev. Mod. Phys., 71, 173
Kogut A., Banday A. J., Bennett C. L., Gorski K. M., Hinshaw G., Smoot G. F., Wright E. I., 1996, ApJ, 464, L5
Kun M., Balog Z., Mizuno N., Kawamura A., Gáspár A., Kenyon S. J., Fukui Y., 2008, MNRAS, 391, 84
Leitch E. M., Readhead A. C. S., Pearson T. J., Myers S. T., 1997, ApJ, 486, L23
Li A., Draine B. T., 2001, ApJ, 554, 778
Maddalena R. J., Morris M., Moscowitz J., Thaddeus P., 1986, ApJ, 303, 375
Murphy E. J. et al., 2010, ApJ, 709, L108
Natoli P., de Gasperis G., Gheller C., Vittorio N., 2001, A&A, 372, 346
Ott M., Witzel A., Quirrenbach A., Krichbaum T. P., Standke K. J., Schalinski C. J., Hummel C. A., 1994, A&A, 284, 331
Paladini R. et al., 2012, ApJ, 760, 149
Peel M. W., Dickinson C., Davies R. D., Banday A. J., Jaffe T. R., Jonas J. L., 2012, MNRAS, 424, 2676
Pilbratt G. L. et al., 2010, A&A, 518, L1
Planck Collaboration XX, 2011, A&A, 536, A20
Planck Collaboration XI 2014, A&A, 571, A11
Planck Collaboration XV, 2014, A&A, 565, A103
Poglitsch A. et al., 2010, A&A, 518, L2
Schultz G. V., Wiemer W., 1975, A&A, 43, 133
Seiffert M., Mennella A., Burigana C., Mandolesi N., Bersanelli M., Meinhold P., Lubin P., 2002, A&A, 391, 1185
Silsbee K., Ali-Haïmoud Y., Hirata C. M., 2011, MNRAS, 411, 2750
Sneden C., Gehrz R. D., Hackwell J. A., York D. G., Snow T. P., 1978, ApJ, 223, 168
Thompson A. R., Moran J. M., Swenson G. W., 2007, Interferometry and Synthesis in Radio Astronomy. Wiley
Tibbs C. T. et al., 2012, ApJ, 754, 94
Tielens A. G. G. M., 2008, ARA&A, 46, 289
Vrba F. J., Rydgren A. E., 1984, ApJ, 283, 123
Vrba F. J., Rydgren A. E., 1985, AJ, 90, 1490
Watson R. A., Rebolo R., Rubiño-Martín J. A., Hildebrandt S., Gutiérrez C. M., Fernández-Cerezo S., Hoyland R. J., Battistelli E. S., 2005, ApJ, 624, L89
Weingartner J. C., Draine B. T., 2001, ApJ, 548, 296
Wright E. L. et al., 2010, AJ, 140, 1868
Ysard N., Miville-Deschênes M. A., Verstraete L., 2010, A&A, 509, L1
Zwart J. T. L. et al., 2008, MNRAS, 391, 1545

APPENDIX A: MAXIMUM LIKELIHOOD MAP MAKING

For this work an independent maximum-likelihood (ML) map maker was developed. The map maker follows the methods outlined in previous ML map-making papers (Natoli et al. 2001; Doré et al. 2001). The goal of ML map making is to iteratively solve for the full noise covariance matrix of the input time-ordered-data (TOD) and remove stripes in the final map caused by $1/f$ noise. The ML map maker used in this paper has been independently developed and implemented in PYTHON[1] with PYTHON-callable FORTRAN libraries, compiled using F2PY.[2] This Appendix briefly discusses simulations used to test the capabilities of the ML map maker to remove $1/f$ noise and recover a known input signal.

Fig. A1 shows an input map that was sampled to generate simulated noiseless TOD. Correlated noise was added to the TOD using the $1/f$ noise model

$$P_\nu = \left(\frac{\sigma}{\nu_s}\right)^2 \left[1 + \left(\frac{\nu_{\rm knee}}{\nu}\right)^\alpha\right], \tag{A1}$$

where σ is the receiver sensitivity, ν_s is the sample rate, $\nu_{\rm knee}$ is the knee frequency, α is spectral index and ν is the frequency of a given spectral bin. The parameters for the simulated noise were chosen to match the noise of the *C*-band GBT data.

Fig. A1 shows how a simulated diffuse source contaminated with $1/f$ can be reliably recovered using the ML map maker. The residual map shows only white noise and a residual dipole. Typically, the ML map maker cannot constrain the absolute background (monopole) and the dipole moment of the map as there is not sufficient information on those scales. However, the effect of the dipole can typically be ignored as only the smaller scale structures within a map are of interest.

For real data, ML map making cannot remove all the effects of $1/f$ noise. This is because the noise in real data will typically be non-stationary meaning the σ, $\nu_{\rm knee}$ and α can all vary with time. The effect of non-stationary noise can be reduced by generating ML maps from subsets of the data where the noise is quasi-stationary. However, splitting the data up is not always possible because the integration time per pixel would be too low or constraints due to the scanning strategy used.

In the case of the GBT data, the observations were split by polarization, as the receiver chains measured either LL or RR polarized emission. Therefore, each polarization would have slightly different noise properties. A map for each polarization was generated and both were averaged to produce the final map. In Fig. A2, a difference map generated from two independent sets of *C*-band data is presented. Each independent set contained *C*-band data from different days of observing. After ML map making, the *C*-band maps were used to generate a difference map that should contain statistically similar $1/f$ noise as the *C*-band map.

Visual inspection of Fig. A2 shows no clear evidence of the same structures seen in the *C*-band data, similar to the difference map of the simulated data in Fig. A1. This implies that there is

[1] Python Software Foundation. Python Language Reference, version 2.7. Available at http://www.python.org
[2] http://sysbio.ioc.ee/projects/f2py2e/

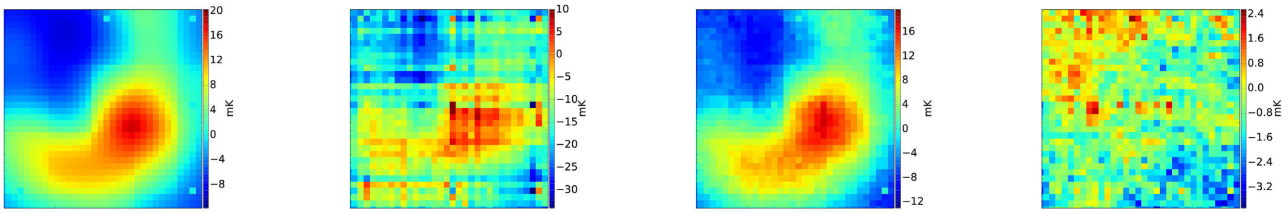

Figure A1. ML map-maker simulations. From left to right the maps show: noiseless input map; input map with $1/f$ noise contamination; recovered map using ML map making; difference between the noiseless input map and recovered map.

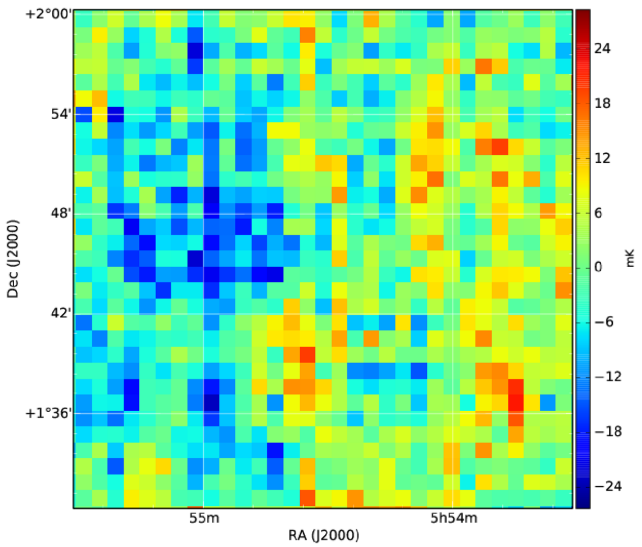

Figure A2. Difference map generated from *C*-band data taken on the first day of observing and *C*-band data taken on the second and third days of observing.

no loss of signal when using ML map making. However, Fig. A2 does show evidence of correlated noise and a gradient that have not been removed by the ML map maker. This is due to the noise, even when the data are split into days with similar weather conditions, being only quasi-stationary. For this reason, it is expected that the sensitivity of the *C*-band and *Ku*-band maps presented in this paper will still contain residual $1/f$ that cannot be reliably removed without degrading the signal from the astronomical source.

This paper has been typeset from a TEX/LATEX file prepared by the author.